




Preparation and property optimization of silver-embedded FTO transparent conductive thin films by laser etching and coating AZO layer

Nai-fei Ren^{1,4}, Wei-zheng Wang^{1,4}, Bao-jia Li^{2,3,4,*} , Li-jing Huang^{1,3,4,*}, and Yao Zhang^{1,4}

¹ School of Mechanical Engineering, Jiangsu University, Zhenjiang 212013, People's Republic of China

² School of Materials Science and Engineering, Jiangsu University, Zhenjiang 212013, People's Republic of China

³ Institute of Micro-Nano Optoelectronic and Terahertz Technology, Jiangsu University, Zhenjiang 212013, People's Republic of China

⁴ Jiangsu Provincial Key Laboratory of Center for Photon Manufacturing Science and Technology, Jiangsu University, Zhenjiang 212013, People's Republic of China

Received: 11 December 2020

Accepted: 7 March 2021

Published online:
22 March 2021

© The Author(s), under exclusive licence to Springer Science+Business Media, LLC, part of Springer Nature 2021

ABSTRACT

Preparation and property optimization of silver (Ag)-embedded fluorine-doped tin oxide (FTO) films were achieved based on laser etching, sputtering Ag layers, furnace annealing, sputtering aluminum-doped zinc oxide (AZO) layers and laser annealing. Specifically, a nanosecond pulsed laser ($\lambda = 532$ nm) was used to etch grooves on FTO films before sputtering 5-nm-thick Ag layers, with an aim for enabling the Ag nanoparticles from the furnace-annealed Ag layers to be intensively embedded in the grooves under the thermal-induced dewetting effect. The optimal laser fluence for laser etching and temperature for furnace annealing were found to be 0.4 J/cm^2 and $300 \text{ }^\circ\text{C}$, respectively. The as-obtained Ag-embedded FTO film exhibited significantly improved optical and electrical properties, being attributed mainly to the decreased coverage area of the Ag nanoparticles on the FTO film surface and the furnace annealing effect. The subsequently sputtered 10-nm-thick AZO layer suppressed the internal light reflection from the Ag nanoparticles, and laser annealing further facilitated grain growth in the film. Therefore, the resulting film had the best comprehensive property with the highest figure of merit of $20.94 \times 10^{-3} \Omega^{-1}$, which was much higher than that of the original FTO film ($7.65 \times 10^{-3} \Omega^{-1}$). This work may provide a new combined processing method for high-performance transparent conductive films.

Address correspondence to E-mail: li_bjia@126.com; lij_huang@126.com

1 Introduction

In recent years, the fluorine-doped tin oxide (FTO) film, with the advantages of low cost and non-toxicity, has been widely used in solar cells [1], light-emitting diodes (LEDs) [2], liquid crystal displays (LCDs) [3], thin film transistors [4], touch screens [5] and other optoelectronic devices. However, the optical and electrical properties of an ordinary FTO film are not sufficient to fully meet the requirements of the evolving optoelectronic devices. It is noticed that preparing a metal/FTO composite film by coating a metal layer and then furnace annealing is one of the more common methods to improve the optical and electrical properties of the FTO film [6, 7]. After furnace annealing, the crystallinity of the film will be enhanced, the grain size will be increased, the defects in the film will be reduced, and thus the optical and electrical properties of the film will be improved [7]. In addition, the metal layer subjected to furnace annealing will form metal nanoparticles through a self-aligned dewetting process [8], and the quantum mechanical tunneling effect and near-field plasma coupling interactions generated by these metal nanoparticles can contribute to further improving the electrical conductivity of the film [9]. However, the optical transmittance of the film will be greatly degraded due to the intense light reflection caused by these densely distributed metal nanoparticles [10]. Similarly, Zhang et al. [11] prepared silver (Ag) nanoparticles on the surfaces of aluminum-doped zinc oxide (AZO) films at room temperature through electrodeposition technology, and found that the denser Ag nanoparticles produced using a longer deposition time resulted in a lower optical transmittance of the film. These results indicated that the metal layer consisting of dense metal nanoparticles would inevitably lead to a light reflection loss and thus lower the optical transparency of the film. Therefore, the preparation of a metal layer-coated FTO film for improving electrical conductivity of the FTO film without sacrificing its optical transmittance is a great challenge and worthy of special exploration.

On the other hand, the AZO film has attracted much attention due to their excellent optical and electrical properties and abundant reserves. Moreover, AZO is an excellent material for preparing the anti-reflection layer of optoelectronic devices, and therefore an AZO layer is usually deposited on the surface of an FTO film to prepare an AZO/FTO

composite film for achieving the purpose of anti-reflection. Although furnace annealing is a common heat treatment method to optimize the quality of transparent conductive oxide (TCO) thin films and improve their optical and electrical properties [12, 13], the AZO film is prone to be ablated and damaged due to the high annealing temperature and the long annealing time in a traditional furnace. To overcome the shortcomings of traditional furnace annealing, laser annealing, as a new annealing method, has gradually emerged and gained popularity due to its gentle thermal budget and short operation time [14–16]. El hamali et al. [17] deposited AZO thin films on quartz substrates by magnetron sputtering and then conducted excimer laser annealing on them, resulting in an enhanced average visible transmittance from 85 to 90% and a reduced resistivity from $1 \times 10^{-3} \Omega \text{ cm}$ to $5 \times 10^{-4} \Omega \text{ cm}$. Huang et al. [18] prepared AZO films on polyethylene terephthalate (PET) flexible substrates by magnetron sputtering and optimized them by nanosecond pulsed laser annealing, achieving the highest average visible transmittance of 76.2% and the lowest resistivity of $1.95 \times 10^{-3} \Omega \text{ cm}$. Therefore, in terms of the metal layer-coated FTO film, it is expected to restrain light reflection from the metal layer by coating an AZO film and optimize the optical and electrical properties of the AZO film by laser annealing.

From the above overview, one can know that the common method of coating metal layer followed by furnace annealing has limitation on simultaneously optimizing optical transmittance and electrical conductivity of the FTO film. The main problem is that the too large coverage area of the metal layer or metal nanoparticles will inevitably cause a significant degradation in optical transmittance of the film. Being inspired by the widely used laser patterning method, we believe that embedding metal nanoparticles into laser-etched grooves on the FTO film is a workable idea for achieving the reduction of their coverage area and thus the improvement of the film transparency. Moreover, as mentioned earlier, the optical transmittance and electrical conductivity of the metal-embedded FTO film can be further optimized by coating AZO layer followed by laser annealing.

In this study, in view of the problem of increasing electrical conductivity and decreasing optical transmittance after furnace annealing of the metal/FTO

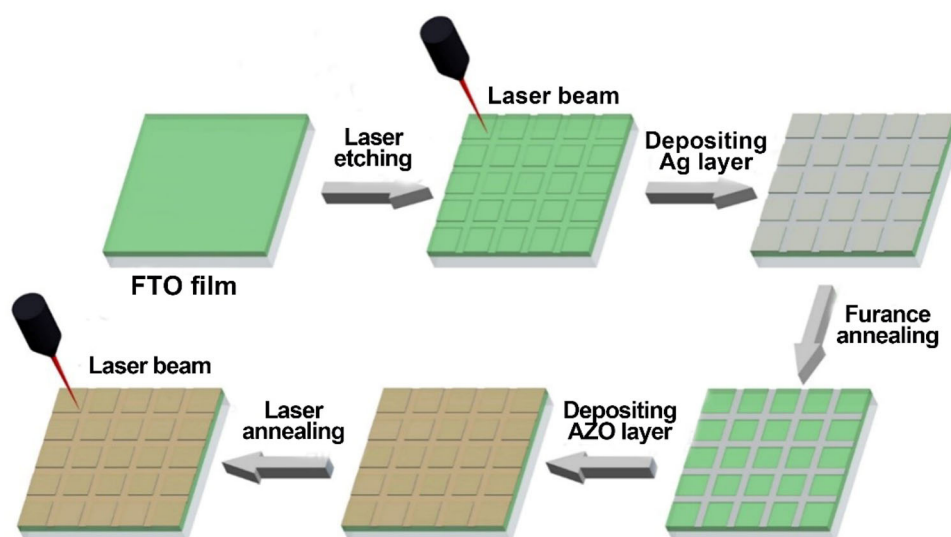
film [10, 11], we used a nanosecond pulsed laser beam ($\lambda = 532$ nm) to etch the FTO film surface before sputtering an Ag layer, with an aim for enabling the Ag nanoparticles from the furnace-annealed Ag layer to be intensively embedded in the laser-etched grooves under the self-aligned dewetting effect. This kind of Ag-embedded FTO film was believed to bring about an improved electrical conductivity, accompanied by a reduced optical transmittance loss that benefited from the decreased coverage area of the Ag nanoparticles on the FTO film surface. On the other hand, to further improve the optical and electrical properties of the Ag-embedded FTO film, an AZO layer was sputtered on the film surface and then annealed by the nanosecond pulsed laser. Specifically, as Fig. 1 shows, the whole preparation process included five steps, i.e., laser etching of the FTO film (FTO_L), depositing an Ag layer on the FTO_L film, furnace annealing of the Ag/FTO_L film, depositing an AZO layer on the Ag/FTO_L film and laser annealing of the AZO/Ag/FTO_L film. The effects of laser fluence during laser etching on the FTO film, annealing temperature during furnace annealing on the Ag/FTO_L film and AZO layer thickness on the AZO/Ag/FTO_L film were mainly investigated to determine the optimal process parameters. The preparation process of the Ag-embedded FTO film may provide a new combined processing method for the research, development and application of high-performance transparent conductive films.

2 Experimental details

2.1 Laser etching of FTO films

The commercially available FTO films (~ 800 nm in thickness) with glass substrates were cut into a square of $15\text{ mm} \times 15\text{ mm}$, and, respectively, immersed in deionized water, acetone and absolute ethanol to be ultrasonically cleaned each for 10 min. The as-cleaned FTO films were then blow-dried using a high-purity (99.999%) nitrogen gun. Subsequently, the FTO films were placed on the sample stage of a diode pumped Nd:YVO₄ nanosecond pulsed laser system (Bright Solutions Co., Ltd., Italy, Wedge532). The laser system mainly consists of a beam expander, a total reflector, a galvanometer system, a focusing lens and a working table. The central wavelength of the laser beam is 532 nm, the pulse width is 1–2 ns, the pulse repetition rate is 1 kHz, and the maximum single pulse energy is 0.9 mJ. Laser etching was performed on the pre-cleaned FTO film surface along the groove grid pattern (400 μm in grid spacing) that was drawn by an EZCAD software in advance. The main laser parameters such as defocusing amount (0 mm), laser fluence (0.2 J/cm², 0.4 J/cm², 0.6 J/cm² and 0.8 J/cm²) and laser scanning speed (10 mm/s) were adjusted by a laser controller that was connected to a computer.

Fig. 1 Preparation flow chart of the Ag-embedded FTO film including laser etching of the FTO film (FTO_L), depositing an Ag layer on the FTO_L film, furnace annealing of the Ag/FTO_L film, depositing an AZO layer on the Ag/FTO_L film and laser annealing of the AZO/Ag/FTO_L film



2.2 Preparation and furnace annealing of Ag/FTO_L films

The laser-etched FTO film (denoted as FTO_L) with the best comprehensive property was chosen to be placed on the sample stage of a radio frequency (RF) magnetron sputtering coating system (Hefei Kejing Material Technology Co., Ltd., China, VTC-2RF) for depositing a 5-nm-thick Ag layer using an Ag target (99.99% purity, $\Phi 50$ mm \times 3 mm). During magnetron sputtering, the deposition chamber was covered with a sealed cover and vacuumed to be cleaned for 5 min using high-purity (99.999%) argon, and then the working pressure and sputtering power were, respectively, controlled at 10 Pa and 30 W. The thickness of the Ag layer was monitored by a quartz crystal-based thickness monitor that was equipped on the coating system. In the next step, the as-prepared Ag/FTO_L film was placed in a medium-temperature tube furnace (Hefei Risine Technology Co., Ltd., China, CVD(Z)-06/60/3) for annealing. Prior to annealing, the tube chamber was cleaned for 5 min using high-purity (99.999%) nitrogen with a constant flow rate of 10 mL/min. The annealing time was fixed at 20 min and different annealing temperatures (200 °C, 300 °C, 400 °C and 500 °C) were adopted.

2.3 Preparation and laser annealing of AZO/Ag/FTO_L films

The furnace-annealed Ag/FTO_L film with the best comprehensive property was chosen to be placed on the sample stage of the RF magnetron sputtering coating system again for depositing an AZO layer using an AZO target (99.99% purity, 3 wt% Al₂O₃, $\Phi 50$ mm \times 3 mm). Different AZO layer thicknesses (5 nm, 10 nm, 15 nm and 20 nm) were employed to optimize the optical and electrical properties of the resulting AZO/Ag/FTO_L films, and the other details were the same as those for depositing the Ag layer. By comparing the comprehensive properties of these AZO/Ag/FTO_L films, the optimal one was determined to undergo laser annealing using the diode pumped Nd:YVO₄ nanosecond pulsed laser system. During laser annealing, the defocusing amount, laser fluence, laser scanning speed and scan line spacing were fixed at +1.5 mm, 0.8 J/cm², 10 mm/s and 20 μ m, respectively.

2.4 Characterization

A confocal laser scanning microscope (CLSM) (Keyence Corp., Japan, VK-X260K) was used to observe the surface morphologies/topography line profiles and obtain the root mean square (RMS) roughness values of the laser-etched FTO films. A field emission scanning electron microscope (FE-SEM) (JEOL Co., Ltd., Japan, JSM-7001F) was utilized to observe the surface morphologies of the Ag/FTO_L and AZO/Ag/FTO_L films. An X-ray diffractometer (XRD) (Bruker Co., Ltd., Germany, D8 Advance) was adopted to determine the crystal structures of all the films. The optical transmittance spectra of the films were measured with an ultraviolet–visible spectrophotometer (Shanghai Metash Instruments Co., Ltd., China, UV-8000). The reflectance spectra of the films were detected using an ultraviolet–visible spectrophotometer (Shanghai Metash Instruments Co., Ltd., China, UV-6100). A digital four-point probe instrument (Guangzhou Four-Point Probes Technology Co., Ltd., China, RTS-9) was employed to test the sheet resistance values of the films.

3 Results and discussion

3.1 Preparation and property optimization of the FTO films with laser-etched grooves

Figure 2 shows the CLSM images and 3D profiles of the laser-etched grooves on the FTO films obtained under laser fluences of 0.2 J/cm², 0.4 J/cm², 0.6 J/cm² and 0.8 J/cm². It could be found that when the laser fluence was small (0.2 J/cm²), as Fig. 2a shows, the surface of the laser-etched groove exhibited the presence of both large circular or elliptic pits formed by the excessive removal of the FTO layer and small pores caused by mixing of air during laser-film interaction. This also implied that the laser energy was effectively absorbed at the FTO/glass and air/FTO interfaces. Actually, as the laser fluence increased to 0.4 J/cm², 0.6 J/cm² and 0.8 J/cm², as Fig. 2b, c and d show, there were no large pits but small pores occurred in the laser-etched groove, indicating that the laser fluence was relatively high and the laser energy absorbed at the air/FTO interface was dominant. In addition, the regions adjacent to the laser-etched groove were grayish black and

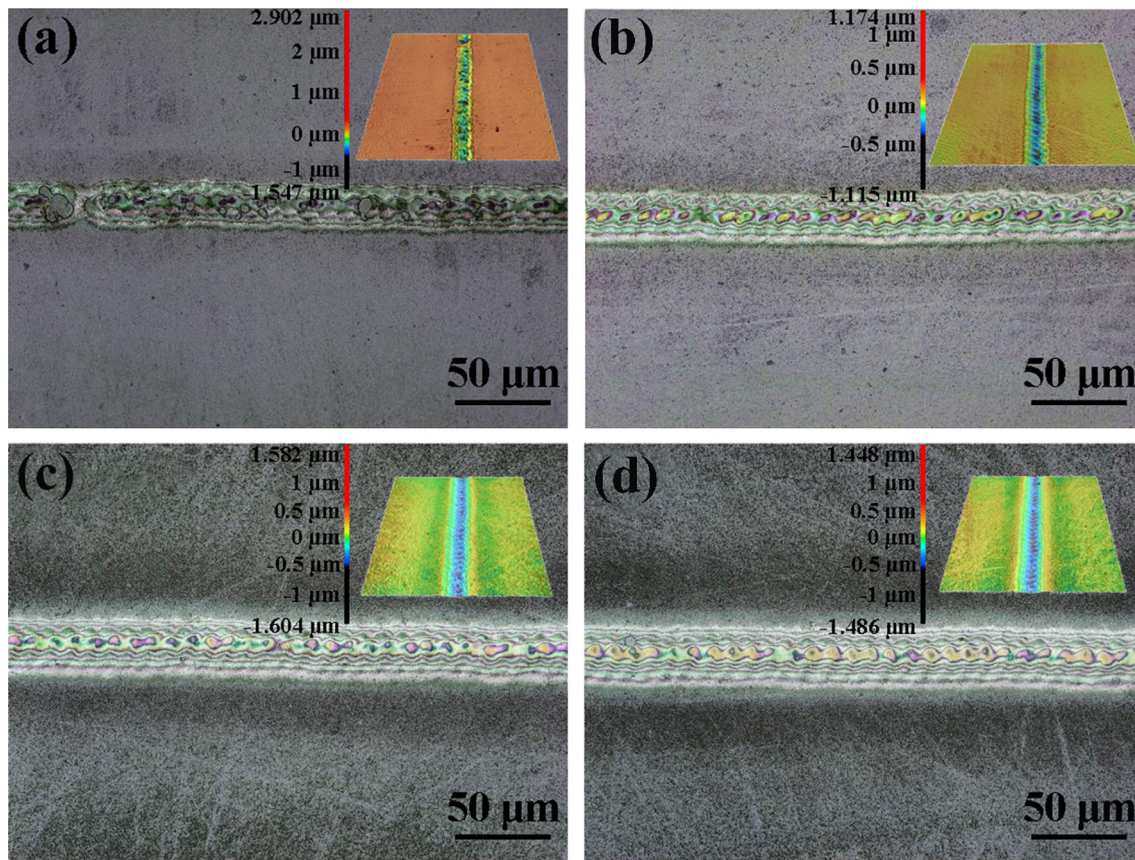


Fig. 2 Confocal laser scanning microscope (CLSM) images of the laser-etched grooves on the FTO films obtained using different laser fluences: **a** 0.2 J/cm²; **b** 0.4 J/cm²; **c** 0.6 J/cm²; **d** 0.8 J/cm². The insets show the corresponding CLSM 3D profiles

extended along the groove, which should be the so-called heat-affected zones caused by the laser-induced thermal effect [19, 20]. The areas of the heat-affected zones were found to become larger with increasing the laser fluence.

Figure 3 presents the typical topography line profiles of the laser-etched grooves on the FTO films obtained under different laser fluences. It was observed that when the laser fluence was relatively low (0.2 J/cm²), the surface of the laser-etched groove had more cone-shaped protrusions due to the laser-caused tearing of the FTO layer. As the laser fluence gradually increased to 0.4 J/cm², 0.6 J/cm² and 0.8 J/cm², the increased laser energy absorbed by the FTO layer enabled it to be melted and thus the number of the cone-shaped protrusions resulted from the FTO layer tearing was significantly reduced. In addition, shoulder-like protrusions could be observed on both sides of the outer edge of the laser-etched groove. These protrusions are believed to be caused by the recoil pressure or pressure waves associated to laser

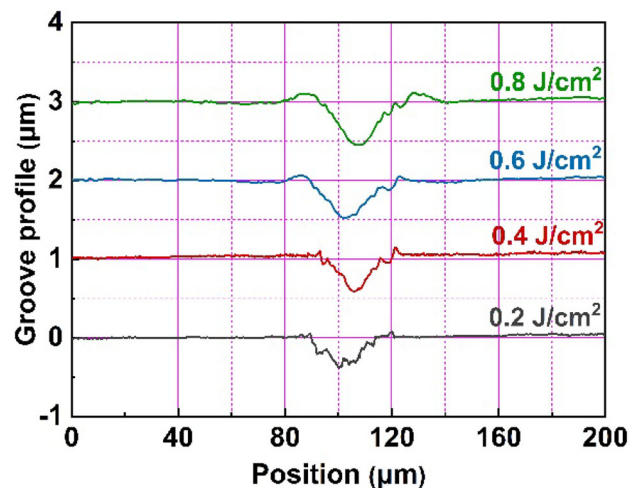


Fig. 3 Typical topography line profiles of the laser-etched grooves on the FTO films obtained using different laser fluences

ablation acting on the molten FTO layer material and pushing it sideways as well as the Marangoni effect generated under surface tension gradients [21–23].

The heights of these protrusions were increased with the increase of laser fluence.

The width, depth and roughness values of these laser-etched grooves were measured by the CLSM, as listed in Table 1. Clear observations were that when the laser fluence increased from 0.2 J/cm² to 0.8 J/cm², the groove width was increased from 26.29 μm to 38.52 μm and the groove depth was increased from 0.38 μm to 0.58 μm. When the laser fluence was relatively low (0.2 J/cm²), only the surface layer of the FTO film was melted under the laser-induced thermal effect, which accordingly resulted in a shallow and narrow groove. With the increase of the laser fluence, the Marangoni convection would occur in the laser-etched area on the FTO film [24]. As a result, the molten FTO layer material would flow toward the low-temperature regions driven by a huge temperature difference, thus bringing about a simultaneous increase in width and depth of the laser-etched groove. Certainly, the high-pressure gases and high-temperature substances generated by the FTO film vaporization would also push the molten FTO layer material into the low-temperature regions, further increasing the groove width and depth [25]. On the other hand, an increase in laser energy would melt a higher volume of FTO layer material and thus produce a wider and deeper track, which should also contribute to the increase in groove width and depth. Under the combined influence of the cone-shaped protrusions, shoulder-like protrusions, pits and pores, the RMS roughness of the laser-etched groove surface was decreased firstly and then increased with the increase of laser fluence. When the laser fluence was 0.4 J/cm², the RMS roughness was the smallest (0.12 μm).

Figure 4a shows the optical transmittance spectra and the corresponding average transmittance values of the unetched FTO film and the laser-etched FTO films obtained using different laser fluences. Due to

the direct interband transitions in these films [26], there were significant decreases in optical transmittance at wavelengths around 300 nm. The average transmittance (T_{av}) values were calculated by averaging the transmittance data within the visible wavelength range of 400–800 nm that could be obtained from the optical transmittance spectra [27], i.e.,

$$T_{av} = \frac{1}{n} \sum_{i=1}^n T_i, \tag{1}$$

where T_i is the transmittance value at a given wavelength and n is the number of the transmittance data in the 400–800 nm waveband. The inset in Fig. 4a revealed that the average transmittance values of the laser-etched FTO films were slightly higher than that of the unetched FTO film (77.18%). This should be ascribed to the partial removal of the FTO layer during the laser etching process [28]. With increasing laser fluence, the width and depth of the laser-etched groove were increased, and therefore the average transmittance of the FTO film was gradually increased. Since the larger groove width and depth means the more FTO layer material removed from the glass substrate, the increase in average transmittance of the FTO film with increasing laser fluence can thus be understood.

Figure 4b displays the sheet resistance histograms of the unetched FTO film and the laser-etched FTO films obtained using different laser fluences. It could be seen that the sheet resistance values of all the laser-etched FTO films were greater than that of the unetched FTO film (9.80 Ω/sq), which resulted from the fact that the FTO conductive layer at the groove was partly removed by the laser and became thinner. Actually, the FTO layer material would be molten and then evaporated under the laser-induced thermal effect. As a result, the physical removal of the laser evaporated FTO material caused the film in the laser-irradiated region to be thinned. On the whole, the sheet resistance values of the laser-etched FTO films exhibited a trend of first decreasing and then increasing with increasing laser fluence. Using a relatively small laser fluence of 0.2 J/cm² led to the largest sheet resistance value (12.04 Ω/sq), which may be related to the generation of the large circular or elliptic pits in the laser-etched grooves that are detrimental to the transportation of the charge carriers [29]. When the laser fluence increased to 0.4 J/

Table 1 Width, depth and RMS roughness values of the laser-etched grooves on the FTO films obtained using different laser fluences

Laser fluence (J/cm ²)	0.2	0.4	0.6	0.8
Width (μm)	26.29	29.10	37.39	38.52
Depth (μm)	0.38	0.40	0.54	0.58
RMS roughness (μm)	0.16	0.12	0.14	0.16

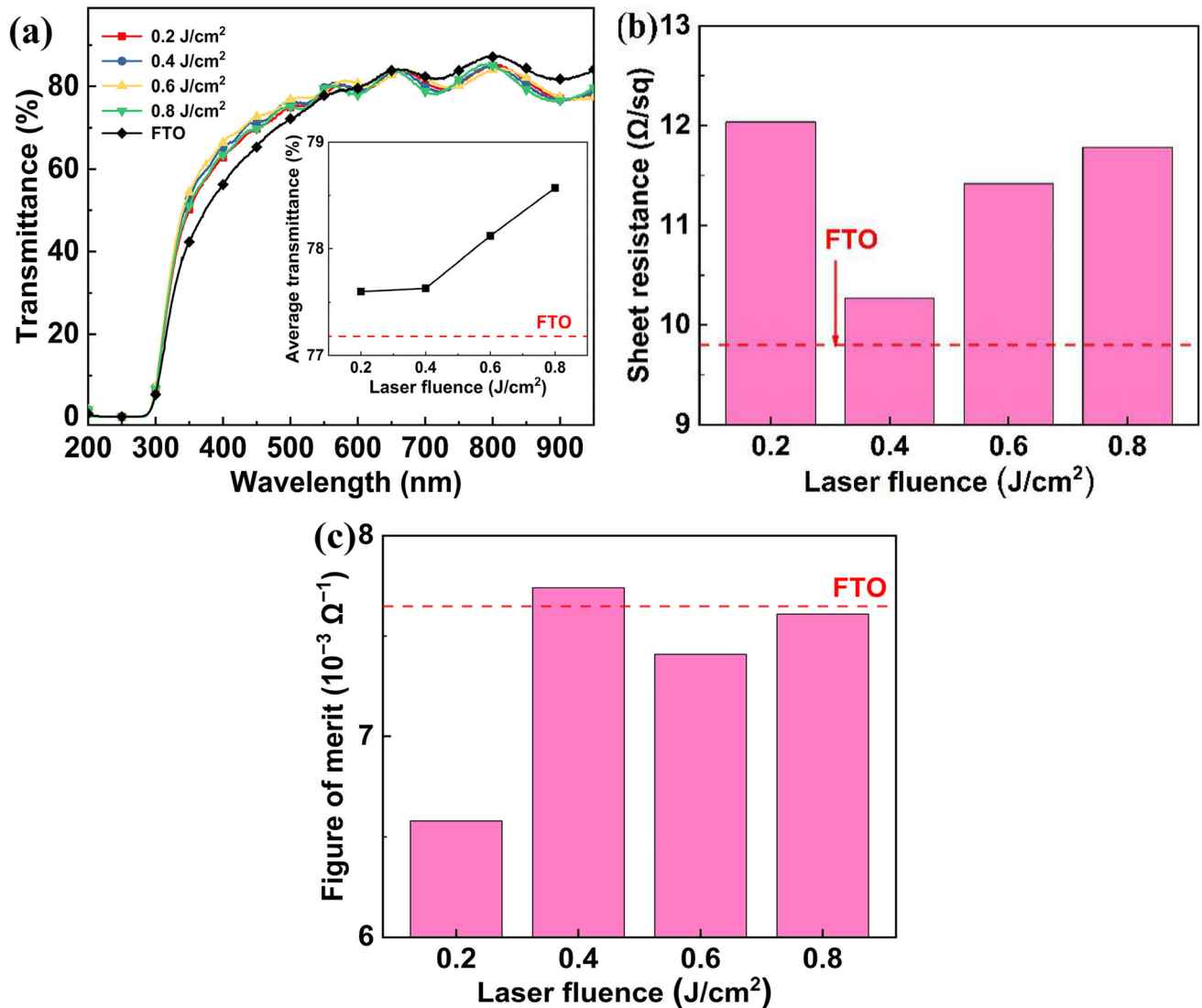


Fig. 4 Optical and electrical properties of the unetched FTO film and the laser-etched FTO films obtained using different laser fluences: **a** optical transmittance spectra and corresponding

cm², as mentioned above, no large pits existed in the laser-etched groove, giving rise to a slightly dropped sheet resistance value of 10.27 Ω/sq. With further increasing laser fluence, the laser-removed width and depth of the FTO layer became enlarged correspondingly, and thus the electrical conductivity was deteriorated as revealed by the gradually increased sheet resistance value. It is well-known that the sheet resistance of a film is inversely proportional to the film thickness. In this present work, the deeper the laser-etched groove on the FTO layer, the smaller the corresponding FTO layer thickness, and hence the larger the sheet resistance value. Since the thinning of the FTO layer during laser etching is a physical

average transmittance values (the inset); **b** sheet resistance values; **c** figure of merit values

removal process, the variation of sheet resistance with laser fluence is just a physical effect.

It was notable that no one film sample simultaneously had the highest transmittance and the lowest sheet resistance, and therefore the comprehensive properties of all the film samples needed to be evaluated by the figure of merit (F_{TC}). According to the Haacke's formula [30], the F_{TC} value of a film sample can be calculated by

$$F_{TC} = \frac{T_{av}^{10}}{R_{sh}} \quad (2)$$

where R_{sh} denotes the sheet resistance value of the film sample. The calculated figures of merit of the

unetched FTO film and the laser-etched FTO films obtained using different laser fluences are shown in Fig. 4c. When the laser fluence was 0.2 J/cm^2 , the resulting laser-etched FTO film had the worst comprehensive property with the lowest figure of merit of $6.58 \times 10^{-3} \Omega^{-1}$. It could be determined that only the laser-etched FTO film using a laser fluence of 0.4 J/cm^2 exhibited the highest figure of merit ($7.74 \times 10^{-3} \Omega^{-1}$) that was higher than that of the unetched FTO film ($7.65 \times 10^{-3} \Omega^{-1}$), suggesting that this film had a better comprehensive property than the unetched FTO film.

3.2 Preparation and property optimization of the furnace-annealed Ag/FTO_L films

According to the above results, the optimal laser fluence for laser etching of the FTO film was determined to be 0.4 J/cm^2 , and therefore the corresponding laser-etched FTO film (FTO_L) was chosen for depositing a 5-nm-thick Ag layer by magnetron sputtering and then undergoing furnace annealing at different annealing temperatures. On the basis of previous studies, the thickness of the Ag layer for preparing the Ag/FTO_L films was set to 5 nm in order to balance their optical transmittance and electrical conductivity [31]. Figure 5 displays the SEM images of the unetched FTO film, the Ag/FTO film annealed at 300 °C for 20 min and the Ag/FTO_L films annealed at different temperatures (200 °C, 300 °C, 400 °C and 500 °C) for 20 min. It could be obviously observed that the surface of the FTO film exhibited pyramid-shaped SnO₂ particles with sharp edges and a sparse distribution (Fig. 5a). The surface of the Ag/FTO film annealed at 300 °C was found to be covered by tiny and sparsely distributed Ag nanoparticles with the underlying relatively large SnO₂ particles (Fig. 5b), which may result from the thermal-induced dewetting effect of the Ag layer and the recrystallization of grains in the FTO layer during furnace annealing [32]. As for the Ag/FTO_L films (Fig. 5c–f), with the increase of annealing temperature, the sizes of both the underlying SnO₂ particles and the upper Ag nanoparticles on the surface of the Ag/FTO_L films increased correspondingly. When the annealing temperature was low (200 °C and 300 °C), the Ag nanoparticles were relatively small and had a relatively dense distribution (Fig. 5c and d). With increasing annealing temperature to 400 °C, the Ag nanoparticles had a slight increase in size (Fig. 5e),

especially inside the laser-etched groove (the inset in Fig. 5e). It is worth noting that when the annealing temperature was too high (500 °C), the Ag nanoparticles displayed a very obvious agglomeration phenomenon [33], and several originally spherical Ag nanoparticles merged into a larger ellipsoidal one (about 200 nm in size) (Fig. 5f). From the insets in Fig. 5c–f, it was found that there were more Ag nanoparticles inside the laser-etched grooves and the Ag nanoparticle size increased with the increase of annealing temperature. The increase in Ag nanoparticle size should be mainly related to the agglomeration of the preformed small Ag nanoparticles under the thermal effect caused by furnace annealing and the well-known Ostwald ripening mechanism [34, 35].

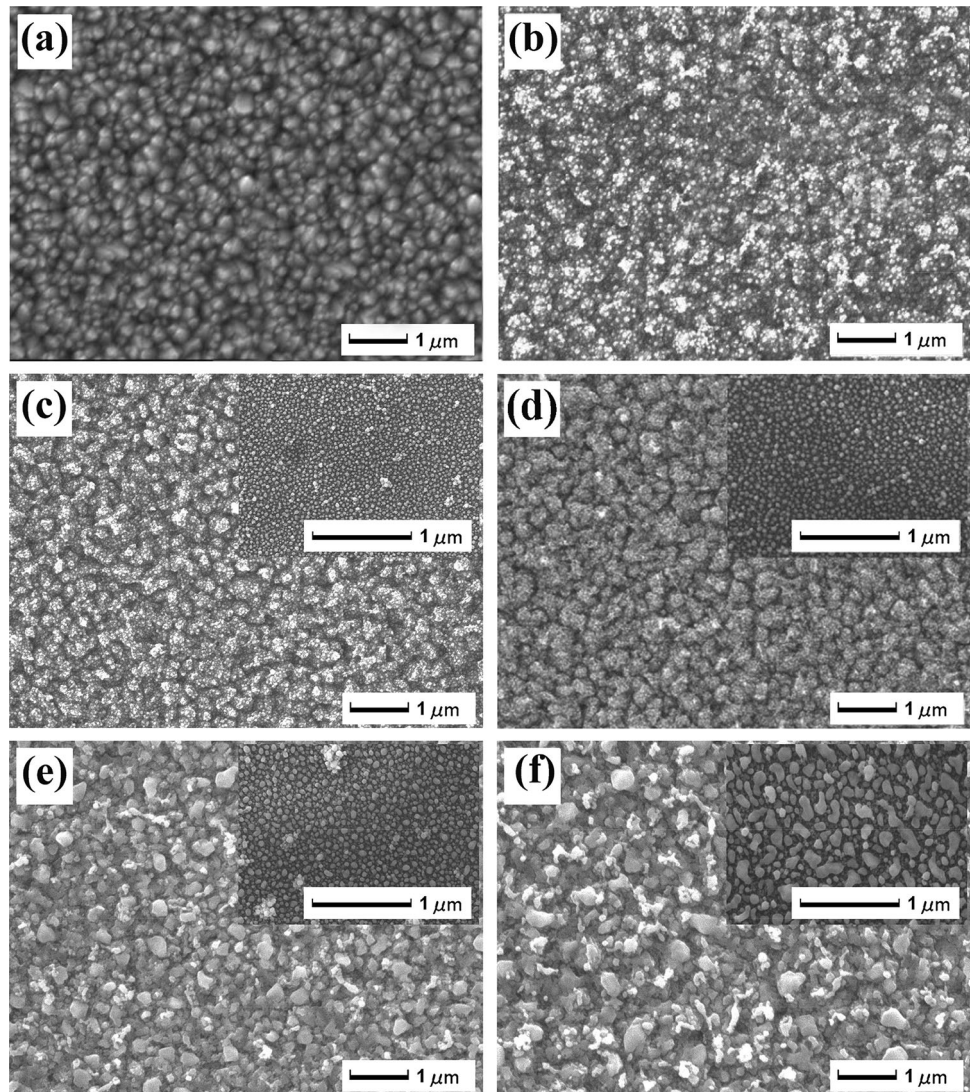
Figure 6 shows the XRD patterns of the Ag/FTO_L films obtained using different annealing temperatures. The XRD patterns of the unetched FTO film and the Ag/FTO film annealed at 300 °C are also shown for comparison. It could be found that all the films showed tetragonal SnO₂ peaks (JCPDS No. 41-1445) [36]. In addition, due to the very thin Ag layer sputtered on the FTO film surface [37, 38], no peaks corresponding to Ag could be observed for all the films. These results confirm the presence of the single-phase SnO₂ [39]. Attributing to the effect of furnace annealing, the SnO₂ (200) peaks of the Ag/FTO film and all the Ag/FTO_L films were stronger than that of the unetched FTO film, and exhibited gradually increased intensities with the increase of annealing temperature [40]. The Ag/FTO and Ag/FTO_L films that were both annealed at 300 °C for 20 min had the similar SnO₂ (200) peak intensities.

According to the XRD data, the grain sizes of the FTO layers can be calculated using the well-known Debye–Scherrer formula defined as follows [41], in order to further study the effect of annealing temperature on the crystal structures of the Ag/FTO_L films.

$$D = \frac{0.9\lambda}{\beta \cos\theta}, \quad (3)$$

where λ is the X-ray wavelength corresponding to the Cu-K α radiation ($\lambda = 0.1541 \text{ nm}$), θ is the Bragg angle, and β is the full width at half maximum (FWHM) of the SnO₂ (200) diffraction peak on the 2θ scale (in radian). The calculated grain sizes are listed in Table 2. As expected, the effect of furnace annealing on grain size was very obvious. During the furnace

Fig. 5 SEM images of **a** the unetched FTO film, **b** the Ag/FTO film annealed at 300 °C and the Ag/FTO_L films annealed at different temperatures: **c** 200 °C; **d** 300 °C; **e** 400 °C; **f** 500 °C. The insets are the SEM images of the surfaces inside the laser-etched grooves on the corresponding films



annealing process, the grain recrystallization within the FTO layer was achieved to produce increased grain sizes, and the higher the temperature, the larger the SnO₂ grains [42]. When the annealing temperature increased from 200 °C to 300 °C, the grain size was significantly increased from 30.85 nm to 43.92 nm. The further increase in annealing temperature to 400 °C or 500 °C only led to a slight increase in grain size (44.76 nm or 45.68 nm). It was noted that the grain sizes of the Ag/FTO and Ag/FTO_L films that were both annealed at 300 °C for 20 min were almost the same, being 43.91 nm and 43.92 nm, respectively.

Figure 7a shows the optical transmittance spectra and the corresponding average transmittance values (400–800 nm waveband) of the unetched FTO film, the Ag/FTO film annealed at 300 °C and the Ag/

FTO_L films annealed at different temperatures. The sharp absorption edges around wavelengths of 300 nm were also observed. It could be found that when the annealing temperature increased from 200 °C to 300 °C, the average transmittance value of the film was increased from 76.39% to 78.40%. This should be ascribed to the significantly increased grain size that can result in a significantly decreased grain-boundary area, and thus a remarkable reduction in scattering loss of the incident light at the grain boundaries [31, 43]. The Ag nanoparticles on the surface of the Ag/FTO_L film annealed at 400 °C (Fig. 5e), as compared to that at 300 °C (Fig. 5d), had a little increase in size and their shape remained regular spherical, and therefore the light trapping effect of the Ag nanoparticles was not weakened obviously. Moreover, the gap area between the Ag

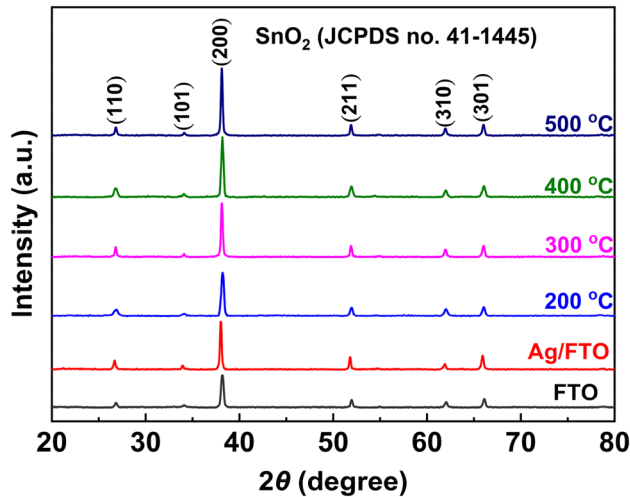


Fig. 6 XRD patterns of the unetched FTO film, the Ag/FTO film annealed at 300 °C and the Ag/FTO_L films annealed at different temperatures

nanoparticles and the SnO₂ grain size had no great difference. All these should be responsible for the slight decrease in average transmittance value (78.28%) of the Ag/FTO_L film annealed at 400 °C. However, when the annealing temperature increased to 500 °C, the size of the Ag nanoparticles on the film surface was increased significantly and their shapes were no longer spherical, which seriously affected the light trapping effect of the Ag nanoparticles. In addition, the excessive temperature might also cause ablation of the film [44]. As a result, although the SnO₂ grain size was increased, it still could not compensate for the loss of optical transmittance, and thus the average transmittance value of the film was dramatically reduced to 76.04%. On the whole, the grain size, the Ag nanoparticle shape and coverage area as well as the excessive temperature-caused ablation should be comprehensively considered for analyzing the variation of average transmittance at different annealing temperatures. Due to the weakening of grain-boundary light scattering, the light trapping effect of Ag nanoparticles and the smaller

coverage area produced by intensively embedding Ag nanoparticles into the laser-etched grooves [45], the average transmittance values of the Ag/FTO_L films annealed at 300 °C and 400 °C were significantly higher than those of the unetched FTO film and the Ag/FTO film annealed at 300 °C.

Figure 7b provides the sheet resistance histograms of the unetched FTO film, the Ag/FTO film annealed at 300 °C and the Ag/FTO_L films annealed at different temperatures. It could be observed that the sheet resistance values of the Ag/FTO film and all the Ag/FTO_L films were smaller than that of the unetched FTO film. These results should be attributed to four aspects. Firstly, the high electrical conductivity of Ag might contribute to electron conduction. Secondly, the effect of furnace annealing resulted in increased SnO₂ grain sizes and thus reduced grain-boundary carrier scattering [27]. Actually, the increase in grain size would cause a decrease in grain-boundary barrier by reducing the grain-boundary area, and thus the number of electrons trapped by the trap level between the grain boundaries would be decreased to bring about a high electrical conductivity [46]. Thirdly, the discontinuously distributed Ag nanoparticles might be conductive under the effects of the quantum mechanical tunneling in the Ag nanoparticles and/or the thermionic electron emission in the FTO layer [9]. Finally, when being exposed to light with a certain wavelength, the Ag nanoparticles might give rise to generating a localized electric field through the near-field plasmonic coupling interactions between adjacent Ag nanoparticles [9, 47]. With regard to all the Ag/FTO_L films, because laser etching would inevitably damage the FTO conductive layer, their sheet resistance values were greater than that of the Ag/FTO film annealed at 300 °C. In addition, the sheet resistance value of the Ag/FTO_L film was decreased from 9.14 to 8.12 Ω/sq as the annealing temperature increased from 200 °C to 400 °C. This should be ascribed to the above second aspect, i.e., the increase

Table 2 Grain sizes of the unetched FTO film, the Ag/FTO film annealed at 300 °C and the Ag/FTO_L films annealed at different temperatures

Sample	FTO	Ag/FTO	Ag/FTO _L				L-AZO/Ag/FTO _L
			200 °C	300 °C	400 °C	500 °C	
Grain size (nm)	29.22	43.91	30.85	43.92	44.76	45.68	44.90

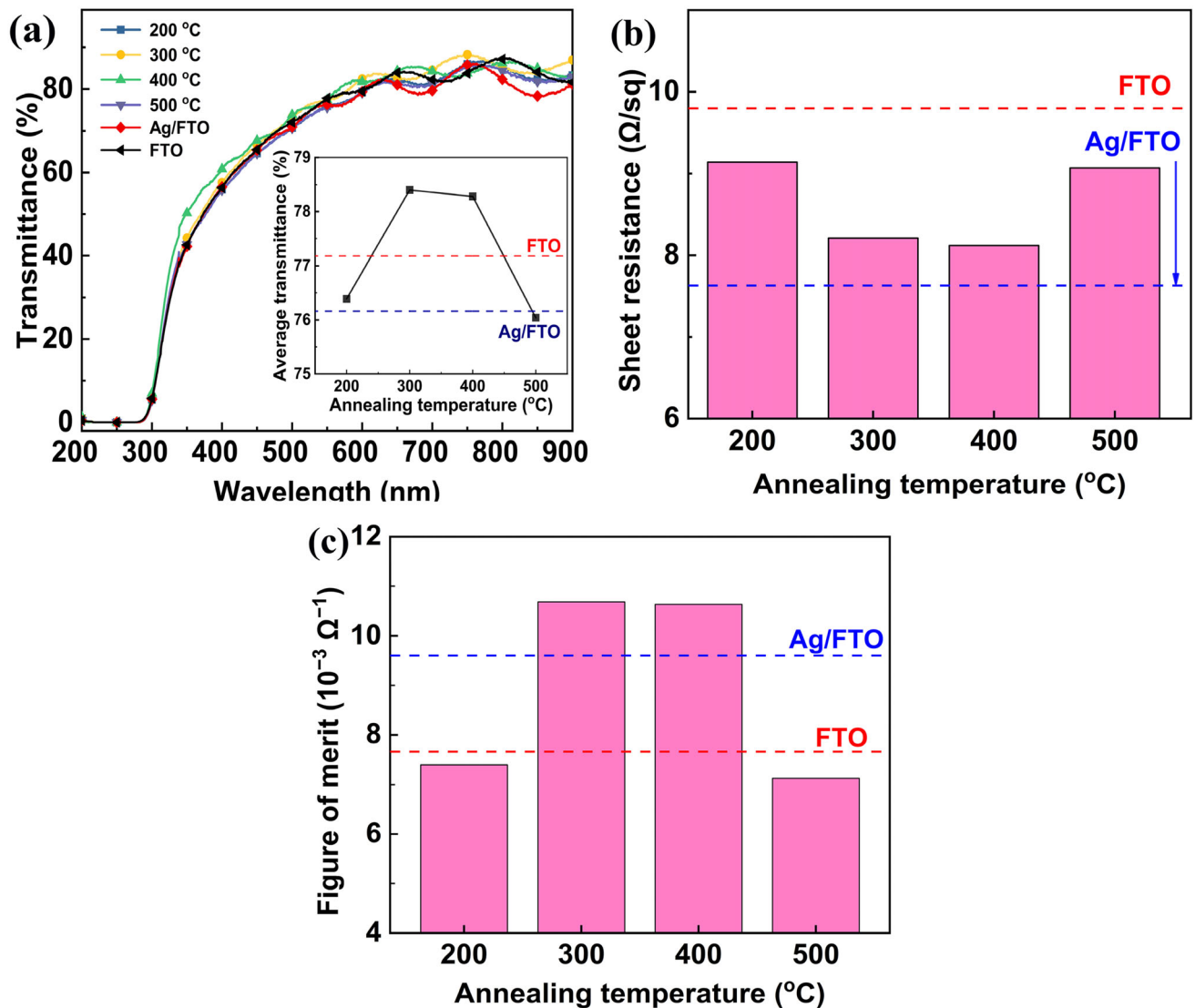


Fig. 7 Optical and electrical properties of the unetched FTO film, the Ag/FTO film annealed at 300 °C and the Ag/FTO_L films annealed at different temperatures: **a** optical transmittance spectra

and corresponding average transmittance values (the inset); **b** sheet resistance values; **c** figure of merit values

in grain size that caused a reduction in grain-boundary carrier scattering. Although the Ag/FTO_L film annealed at 500 °C had the largest grain size (45.68 nm), its sheet resistance value was slightly increased. The agglomerated ellipsoidal Ag particles could broaden the dipole resonance to excite more intense multipole resonance and weaken the electromagnetic field effect [33, 48]. The aforementioned excessive temperature-caused ablation of the film might result in lattice distortion that would be detrimental to carrier transportation [28]. These can provide the explanation for the slight increase in sheet resistance of the Ag/FTO_L film annealed at 500 °C.

To comprehensively evaluate the film performance and determine the parameters for preparing the FTO-based film with the best comprehensive property, the figure of merit values of the unetched FTO film, the Ag/FTO film annealed at 300 °C and the Ag/FTO_L films annealed at different temperatures were calculated using Eq. (2) and the results are shown in Fig. 7c. It could be found that the figure of merit values of the Ag/FTO_L films were increased at first and then decreased with the increase of annealing temperature, and those of the Ag/FTO_L films annealed at 300 °C and 400 °C were obviously greater than of the unetched FTO film and the Ag/

FTO film annealed at 300 °C. The Ag/FTO_L film annealed at 300 °C was found to have the largest figure of merit value ($10.69 \times 10^{-3} \Omega^{-1}$), confirming that this film possessed the best comprehensive property.

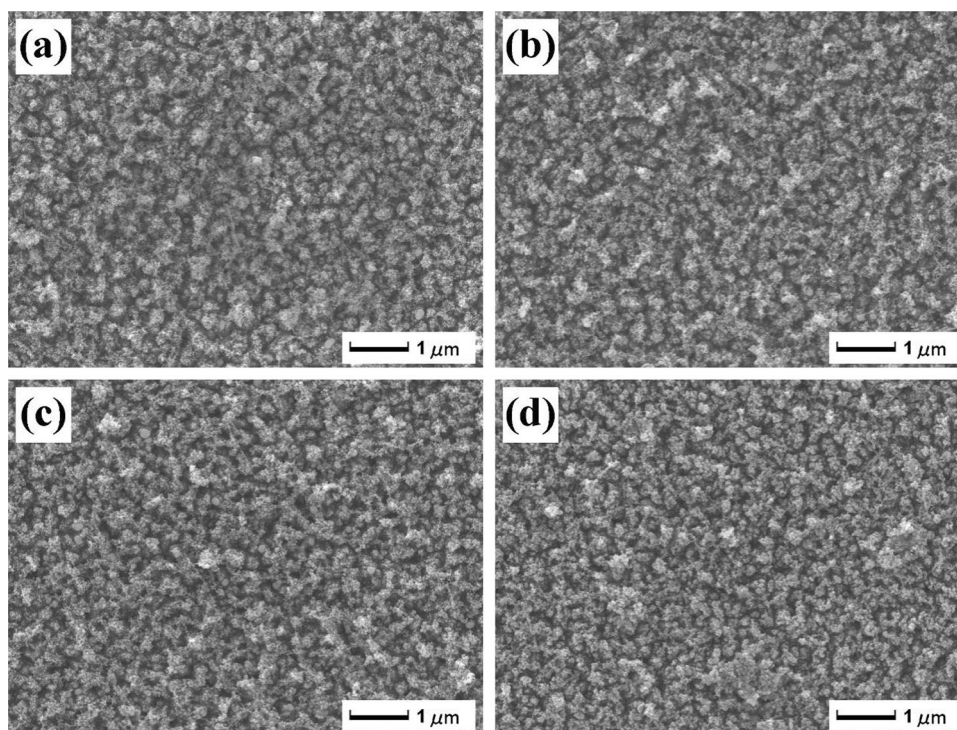
3.3 Preparation and property optimization of the AZO/Ag/FTO_L films

According to the above results, the optimal temperature for furnace annealing of the Ag/FTO_L film was determined to be 300 °C, and therefore the corresponding furnace-annealed Ag/FTO_L film (denoted as F-Ag/FTO_L) was chosen for depositing AZO layers with different thicknesses by magnetron sputtering and then undergoing laser annealing. Figure 8 displays the SEM images of the surfaces outside the laser-etched grooves on the AZO/Ag/FTO_L films with different AZO layer thicknesses. It could be seen that after coating the AZO layers, gray fine ZnO spherical particles appeared on the film surfaces, which were tightly attached to the SnO₂ particles and the Ag nanoparticles. When the thickness of the AZO layer was smaller (5 nm), the number of the ZnO particles was smaller, the distribution was sparse and the size was smaller. It is well-known that the enough AZO material supply during magnetron sputtering

that corresponds to a larger AZO layer thickness is essential to the large and dense ZnO particles. Therefore, the formation of the sparsely distributed and smaller-sized ZnO particles under the smaller AZO layer thickness should be due to the insufficient AZO material supply. As the AZO layer thickness increased, the AZO material became relatively sufficient and thus the ZnO particles were increased significantly, the distribution was denser, and the size was larger. When the AZO layer thickness reached 20 nm, the ZnO particles on the surface of the AZO/Ag/FTO_L film were closely arranged with very few interstices to form a continuous layer (Fig. 8d). These results are similar to those reported by Kumar et al. [49] concerning the dependence of ZnS film density on film thickness (determined by chemical bath deposition time).

The SEM image of the Ag nanoparticles inside a laser-etched groove on the AZO/Ag/FTO_L film with the AZO layer thickness of 10 nm, along with the qualitative illustration for the scattering effect of an Ag nanoparticle on the incident light, are shown in Fig. 9. From Fig. 9a, it could be observed that the sputtered AZO layer became some smaller particles (about 20 nm in size) and combined with the Ag nanoparticles to form a kind of core structure, that is, an Ag nanoparticle with a diameter of about 110 nm

Fig. 8 SEM images of the surfaces outside the laser-etched grooves on the AZO/Ag₅/FTO_L films prepared using different AZO layer thicknesses: **a** 5 nm; **b** 10 nm; **c** 15 nm; **d** 20 nm



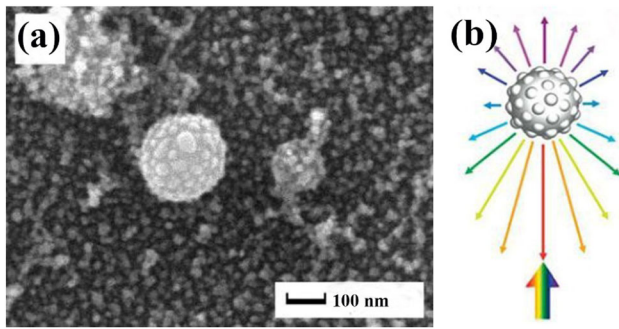


Fig. 9 **a** SEM image of the Ag nanoparticles inside a laser-etched groove on the AZO/Ag/FTO_L film with an AZO layer thickness of 10 nm. **b** A qualitative illustration for the effect of an Ag nanoparticle on incident light scattering (the color arrows are used to illustrate the broadband scattering of the Ag nanoparticle only) (color figure online)

was located in the structure center to become the core, and some smaller ZnO particles were uniformly adhered on the Ag nanoparticle surface. This kind of core structure could contribute to the broadband and wide-angle light scattering, as illustrated in Fig. 9b. This will be discussed later.

Figure 10a provides the optical transmittance spectra and the corresponding average transmittance values (400–800 nm waveband) of the unetched FTO film, the F-Ag/FTO_L film and the AZO/Ag/FTO_L films with different AZO layer thicknesses. The sharp absorption edges still appeared at wavelengths of about 300 nm, indicating that coating an AZO layer had no effect on the interband absorption of the films. On the whole, the average transmittance values of the AZO/Ag/FTO_L films were firstly increased and then decreased with the increase of AZO layer thickness. It

was more obvious that when the AZO layer thickness was smaller (5 nm, 10 nm and 15 nm), the average transmittance value (78.87%, 79.49%, and 79.24%) of the AZO/Ag/FTO_L film was higher than that of the F-Ag/FTO_L film (78.40%). When the AZO layer was relatively thick (20 nm), the continuous AZO layer formed on the film surface could cause a significant decrease in optical transmittance due to the thickness effect [50], and thus the average transmittance of the film was lower than that of the F-Ag/FTO_L film. However, the average transmittance values of all the AZO/Ag/FTO_L films were higher than that of the unetched FTO film.

The reason that the average transmittance values of the AZO/Ag/FTO_L films with AZO layer thicknesses of 5 nm, 10 nm and 15 nm was higher than that of the F-Ag/FTO_L film can be presented as follows. On the one hand, the AZO layer can suppress the internal light reflection from the Ag nanoparticles to achieve an anti-reflection effect [6, 51]. Figure 10b shows the optical reflectance spectra and the corresponding average reflectance values (400–800 nm waveband) of the unetched FTO film, the F-Ag/FTO_L film and the AZO/Ag/FTO_L films with different AZO layer thicknesses. A clear observation was that the average reflectance values of all the AZO/Ag/FTO_L films were lower than those of the FTO film (9.42%) and the F-Ag/FTO_L film (8.54%) and decreased with the increase of AZO layer thickness. These results implied that the reflection of the AZO/Ag/FTO_L films to the incident light was suppressed and thereby the optical transmittance of the films was improved. On the other hand, the core structure demonstrated above had a larger Ag nanoparticle as

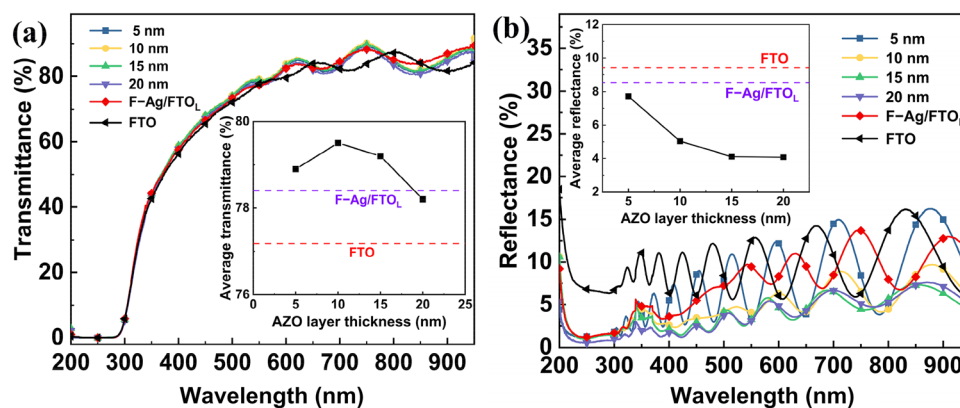


Fig. 10 Optical properties of the unetched FTO film, the F-Ag/FTO_L film and the AZO/Ag/FTO_L films prepared using different AZO layer thicknesses: **a** optical transmittance spectra and

corresponding average transmittance values (the inset); **b** optical reflection spectra and corresponding average reflectance values (the inset)

the core (Fig. 9b), which might excite the dipole and quadrupole plasmon modes, making the incident light in the long-wavelength region have larger scattering coefficients. Most significantly, the small-sized ZnO particles that wrapped the inner core could act as large-angle scatterers for the short-wavelength incident light [52, 53]. Therefore, this core structure could strongly scatter the incident light in a wide wavelength range. The scattered light would be redirected by the convex spherical surface of the core structure for preferentially scattering out of the film, thereby contributing to the improvement in optical transmittance of the AZO/Ag/FTO_L films.

Figure 11a gives the sheet resistance histograms of the unetched FTO film, the F-Ag/FTO_L film and the AZO/Ag/FTO_L films with different AZO layer thicknesses. The sheet resistance values of all the AZO/Ag/FTO_L films were found to be smaller than that of the unetched FTO film (9.80 Ω/sq). As discussed before, the electrical conductivity of the F-Ag/FTO_L film was better than that of the unetched FTO film, and therefore coating the conductive AZO layer on the F-Ag/FTO_L film would further enable the electrical conductivity to be enhanced [54]. In addition, the sheet resistance values of these AZO/Ag/FTO_L films were greater than that of the F-Ag/FTO_L film (8.21 Ω/sq). The presence of the ZnO particles could certainly result in restriction of the quantum mechanical tunneling effect in the excited Ag nanoparticles and the localized electric field caused by plasmonic coupling between Ag nanoparticles [47, 55], which should be responsible for the decline in electrical conductivity of the AZO/Ag/FTO_L films. This restriction would be particularly dominant when the AZO layer thickness was large enough to form a continuous layer, and therefore the electrical conductivity of the AZO/Ag/FTO_L film with the

AZO layer thickness of 20 nm was obviously weakened, displaying a sheet resistance value of 8.71 Ω/sq. However, due to the small number and sparse distribution of the ZnO particles on the AZO/Ag/FTO_L films with smaller AZO layer thicknesses (5 nm, 10 nm and 15 nm), coating the AZO layers had no obvious effect on their electrical conductivity. Therefore, their sheet resistance values only exhibited slight increases.

To determine and compare the comprehensive properties of the unetched FTO film, the F-Ag/FTO_L film and the AZO/Ag/FTO_L films with different AZO layer thicknesses, their figure of merit values calculated using Eq. (2) are shown in Fig. 11b. It could be clearly seen that the figure of merit values of all the AZO/Ag/FTO_L films were greater than that of the unetched FTO film. When the AZO layer thickness was 5 nm, the figure of merit value was $11.27 \times 10^{-3} \Omega^{-1}$. As the AZO layer thickness increased to 10 nm, the figure of merit value reached the maximum ($12.09 \times 10^{-3} \Omega^{-1}$), which was greater than those of the unetched FTO film and the F-Ag/FTO_L film. Further increasing AZO layer thickness led to decreases in figure of merit value, and even produced a figure of merit value of $9.76 \times 10^{-3} \Omega^{-1}$ that was smaller than that of the F-Ag/FTO_L film as the AZO layer thickness increased to 20 nm. It can thus be determined that the AZO/Ag/FTO_L film with an AZO layer thickness of 10 nm had the best comprehensive property.

According to the above results, the optimal AZO layer thickness was determined to be 10 nm, and therefore the corresponding AZO/Ag/FTO_L film was chosen for laser annealing (denoted as L-AZO/Ag/FTO_L film). The SEM image of the L-AZO/Ag/FTO_L film is shown in Fig. 12a. It could be obviously observed that the particles on the surface outside the

Fig. 11 **a** Sheet resistance values and **b** figure of merit values of the unetched FTO film, the F-Ag/FTO_L film and the AZO/Ag/FTO_L films prepared using different AZO layer thicknesses

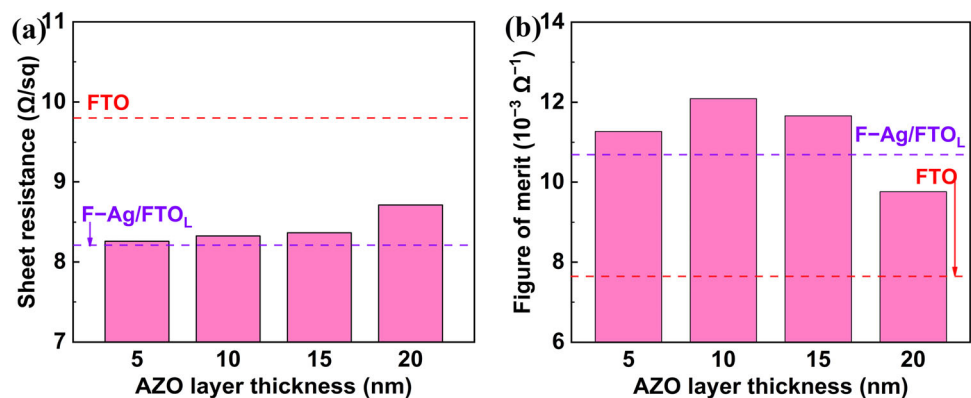
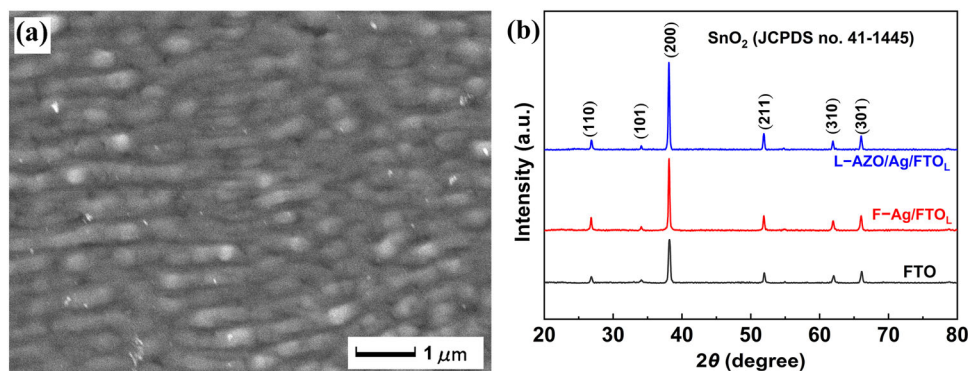


Fig. 12 **a** SEM image of the L-AZO/Ag/FTO_L film; **b** XRD patterns of the unetched FTO film, the F-Ag/FTO_L film and the L-AZO/Ag/FTO_L film

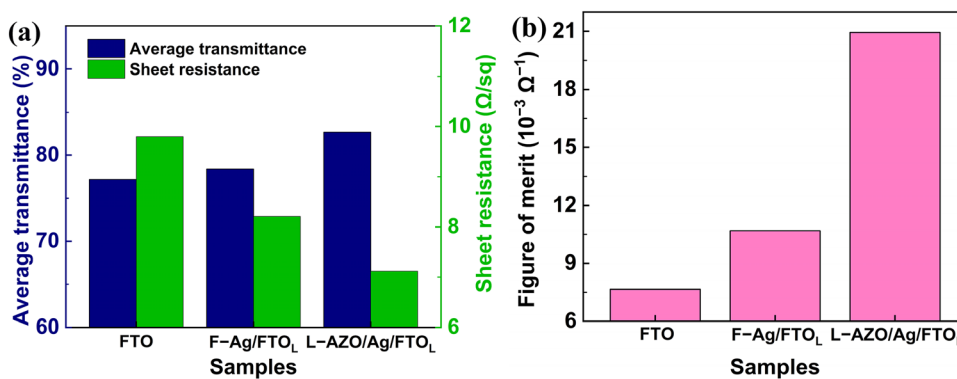


laser-etched groove were melted and recrystallized into long strip shapes under the laser-induced thermal effect, showing a grating-like structure. The XRD pattern of the L-AZO/Ag/FTO_L film is provided in Fig. 12b, along with those of the unetched FTO film and the F-Ag/FTO_L film for comparison. The L-AZO/Ag/FTO_L film also showed the tetragonal SnO₂ peaks (JCPDS No. 41-1445) without Ag peaks that were the same as those of the unetched FTO film and the F-Ag/FTO_L film. It is worth noting that the SnO₂ (200) peak intensity of the L-AZO/Ag/FTO_L film was significantly higher than those of the unetched FTO film and the F-Ag/FTO_L film, which verified that laser annealing could enhance the film crystallinity. The grain size of the L-AZO/Ag/FTO_L film calculated using Eq. (3) is also listed in Table 2. The L-AZO/Ag/FTO_L film had a relatively large grain size of 44.90 nm as compared to the unetched FTO film (29.22 nm) and the F-Ag/FTO_L film (43.92 nm), indicating that laser annealing further facilitated grain growth in the film [56].

The average transmittance and sheet resistance values of the unetched FTO film, the F-Ag/FTO_L film and the L-AZO/Ag/FTO_L film are displayed in Fig. 13a. It could be found that both the average

transmittance (82.67%) and the sheet resistance (7.12 Ω/sq) of the L-AZO/Ag/FTO_L film were obviously improved compared to the unetched FTO film and the F-Ag/FTO_L film. This was believed to mainly result from the enlarged grains after laser annealing that could reduce the grain-boundary light and carrier scattering losses [57]. Kumar et al. [58] have also reported an increase in optical transmittance originated from the increase in grain size. Certainly, the grating-like structure on the L-AZO/Ag/FTO_L film might also play a role in enhancing its optical transmittance through anti-reflection effect [51]. Figure 13b presents the figure of merit values of the unetched FTO film, the F-Ag/FTO_L film and the L-AZO/Ag/FTO_L film. It could be directly determined that the L-AZO/Ag/FTO_L film had the best comprehensive property, showing a figure of merit value of $20.94 \times 10^{-3} \Omega^{-1}$ that was much higher than those of the unetched FTO film and the F-Ag/FTO_L film. This work may provide an effective approach for developing high-performance Ag-embedded FTO-based films.

Fig. 13 Optical and electrical properties of the unetched FTO film, the F-Ag/FTO_L film and the L-AZO/Ag/FTO_L film: **a** average transmittance and sheet resistance values; **b** figure of merit values



4 Conclusion

Ag-embedded FTO films were prepared by laser etching of FTO films (FTO_L), magnetron sputtering of 5-nm-thick Ag layer on the FTO_L films (Ag/FTO_L) and furnace annealing of the Ag/FTO_L films (F-Ag/FTO_L). The results showed that laser-etched grooves without large pits but shoulder-like protrusions were produced at a laser fluence of 0.4 J/cm². The corresponding FTO_L film had the smallest RMS roughness of 0.12 μm and the highest figure of merit of $7.74 \times 10^{-3} \Omega^{-1}$. The furnace annealing of the F-Ag/FTO_L film at 300 °C resulted in the formation of relatively small and densely distributed Ag nanoparticles intensively embedded into the laser-etched grooves. The resulting F-Ag/FTO_L film exhibited the largest grain size of 43.92 nm and the highest figure of merit of $10.69 \times 10^{-3} \Omega^{-1}$. The further property optimization of the F-Ag/FTO_L film by depositing AZO layers (AZO/Ag/FTO_L) showed the increased number, density and size of the ZnO particles with increasing AZO layer thickness, and a kind of core structure was observed inside the laser-etched groove at an AZO layer thickness of 10 nm. Laser annealing of the AZO/Ag/FTO_L film (L-AZO/Ag/FTO_L) led to the formation of a grating-like structure with an increased grain size of 44.90 nm, thus achieving the best comprehensive property with an average transmittance of 82.67%, a sheet resistance of 7.12 Ω/sq and a figure of merit of $20.94 \times 10^{-3} \Omega^{-1}$. This work is expected to provide some valuable reference for improving the comprehensive property of TCO-based films.

Acknowledgements

This work was financially supported by the National Natural Science Foundation of China (Grant nos. 51805220 and 61405078). The authors would like to thank the support of the Young Backbone Teacher Cultivating Project of Jiangsu University (Reference no. 5521220008).

References

1. C. Ma, X. Lu, B. Xu, F. Zhao, X. An, B. Li, L. Sun, J. Jiang, Y. Chen, J. Chu, Effects of sputtering parameters on photoelectric properties of AZO film for CZTS solar cell. *J. Alloys Compd.* **774**, 201–209 (2019)
2. J.N. Alexander, N. Sun, R. Sun, H. Efstathiadis, P. Haldar, Development and characterization of transparent and conductive InZnO films by magnetron sputtering at room temperature. *J. Alloys Compd.* **633**, 157–164 (2015)
3. F. Mei, T. Yuan, A. Chu, R. Li, Comparative study on the microstructure and properties of 10 wt%- and 35 wt%-tin doped indium oxide materials. *J. Eur. Ceram. Soc.* **39**, 4806–4816 (2019)
4. R. Li, S. Dai, Y. Ma, L. Tian, Q. Wang, D. Zhou, X. Zhang, High-performance transparent Li-doped indium-tin-zinc-oxide thin film transistor fabricated by radio frequency magnetron sputtering method. *Mater. Lett.* **230**, 132–134 (2018)
5. W. Zhang, J. Xiong, L. Liu, X. Zhang, H. Gu, Influence of annealing temperature on structural, optical and electrical properties of AZO/Pd/AZO films. *Sol. Energy Mater. Sol. Cells* **153**, 52–60 (2016)
6. B.J. Li, L.J. Huang, N.F. Ren, X. Kong, Y.L. Cai, J.L. Zhang, Superhydrophobic and anti-reflective ZnO nanorod-coated FTO transparent conductive thin films prepared by a three-step method. *J. Alloys Compd.* **674**, 368–375 (2016)
7. L.J. Huang, B.J. Li, H.D. Cao, W. Zu, N.F. Ren, H. Ding, Influence of annealing temperature on formation and photoelectric properties of AZO nanosheet-coated FTO-based films. *J. Mater. Sci. - Mater. Electron.* **28**, 4706–4712 (2017)
8. K.C. Lee, S.J. Lin, C.H. Lin, C.S. Tsai, Y.J. Lu, Size effect of Ag nanoparticles on surface plasmon resonance. *Surf. Coat. Technol.* **202**, 5339–5342 (2008)
9. L.J. Huang, G.M. Zhang, Y. Zhang, B.J. Li, N.F. Ren, L. Zhao, Y.L. Wang, Preparation and photoelectric properties of patterned Ag nanoparticles on FTO/glass substrate by laser etching and driving layer strategy. *Acta Metall. Sin. Engl. Lett.* (2020). <https://doi.org/10.1007/s40195-020-01169-y>
10. M. Li, Y. Wang, Y. Wang, X. Wei, AZO/Ag/AZO transparent flexible electrodes on mica substrates for high temperature application. *Ceram. Int.* **43**, 15442–15446 (2017)
11. D. Zhang, Y. Tang, F. Jiang, Z. Han, J. Chen, Electrodeposition of silver nanoparticle arrays on transparent conductive oxides. *Appl. Surf. Sci.* **369**, 178–182 (2016)
12. C.F. Ding, W.T. Hsiao, H.T. Young, Evaluation of structural properties of AZO conductive films modification using low-temperature ultraviolet laser annealing. *Ceram. Int.* **45**, 16387–16398 (2019)
13. L. Dejam, S.M. Elahi, H.H. Nazari, H. Elahi, S. Solaymani, A. Ghaderi, Structural and optical characterization of ZnO and AZO thin films: the influence of post-annealing. *J. Mater. Sci. - Mater. Electron.* **27**, 685–696 (2016)
14. C.T. Angelis, C.A. Dimitriadis, M. Miyasaka, F.V. Farmakis, G. Kamarinos, J. Brini, J. Stoemenos, Effect of excimer laser

- annealing on the structural and electrical properties of polycrystalline silicon thin-film transistors. *J. Appl. Phys.* **86**, 4600–4606 (1999)
15. Y. Zhao, Y. Jiang, Effect of KrF excimer laser irradiation on the properties of ZnO thin films. *J. Appl. Phys.* **103**, 114903 (2008)
 16. T. Shimogaki, T. Ofuji, N. Tetsuyama, K. Okazaki, M. Higashihata, D. Nakamura, H. Ikenoue, T. Asano, T. Okada, Effect of laser annealing using high repetition rate pulsed laser on optical properties of phosphorus-ion-implanted ZnO nanorods. *Appl. Phys. A.* **114**, 625–629 (2014)
 17. S.O. El hamali, W.M. Cranton, N. Kalfagiannis, X. Hou, R. Ranson, D.C. Koutsogeorgis, Enhanced electrical and optical properties of room temperature deposited Aluminium doped Zinc Oxide (AZO) thin films by excimer laser annealing. *Opt. Lasers Eng.* **80**, 45–51 (2016)
 18. L.J. Huang, B.J. Li, N.F. Ren, Enhancing optical and electrical properties of Al-doped ZnO coated polyethylene terephthalate substrates by laser annealing using overlap rate controlling strategy. *Ceram. Int.* **42**, 7246–7252 (2016)
 19. N.F. Ren, H.D. Cao, L.J. Huang, B.J. Li, W. Zu, Ultrasonic-vibration-assisted laser annealing on photoelectric properties of FTO thin films. *J. Inorg. Mater. Chin. Ed.* **32**, 1083–1088 (2017)
 20. Y.L. Wang, B.J. Li, S.S. Li, H. Li, L.J. Huang, N.F. Ren, Parameter optimization in femtosecond pulsed laser etching of fluorine-doped tin oxide films. *Opt. Laser Technol.* **116**, 162–170 (2019)
 21. A.N. Samant, N.B. Dahotre, Differences in physical phenomena governing laser machining of structural ceramics. *Ceram. Int.* **35**, 2093–2097 (2009)
 22. J. Hoffman, The effect of recoil pressure in the ablation of polycrystalline graphite by a nanosecond laser pulse. *J. Phys. D: Appl. Phys.* **48**, 235201 (2015)
 23. C. Tang, K.Q. Le, C.H. Wong, Physics of humping formation in laser powder bed fusion. *Int. J. Heat Mass Transfer* **149**, 119172 (2020)
 24. S.-F. Tseng, W.-T. Hsiao, K.-C. Huang, D. Chiang, The effect of laser patterning parameters on fluorine-doped tin oxide films deposited on glass substrates. *Appl. Surf. Sci.* **257**, 8813–8819 (2011)
 25. J. Berger, T. Roch, S. Correia, J. Eberhardt, A.F. Lasagni, Controlling the optical performance of transparent conducting oxides using direct laser interference patterning. *Thin Solid Films* **612**, 342–349 (2016)
 26. X.Q. Wang, L.L. Fan, Z.S. Wang, J.B. Gong, J.W. Hou, R.C. Dai, Z.P. Wang, C.E. Zou, Z.M. Zhang, Exact interband transition energies of VO₂ films. *Thin Solid Films* **645**, 160–165 (2018)
 27. B.J. Li, G.Y. Yang, L.J. Huang, W. Zu, N.F. Ren, Performance optimization of SnO₂: F thin films under quasi-vacuum laser annealing with covering a transparent PET sheet: a study using processing map. *Appl. Surf. Sci.* **509**, 145334 (2020)
 28. B.J. Li, H. Li, L.J. Huang, H.D. Cao, W. Zu, N.F. Ren, H. Ding, X. Kong, J.L. Zhang, Performance optimization of fluorine-doped tin oxide thin films by introducing ultrasonic vibration during laser annealing. *Ceram. Int.* **43**, 7329–7337 (2017)
 29. H.B. Lee, W.Y. Jin, M.M. Ovhall, N. Kumar, J.W. Kang, Flexible transparent conducting electrodes based on metal meshes for organic optoelectronic device applications: A review. *J. Mater. Chem. C* **7**, 1087–1110 (2019)
 30. K.-L. Wang, Y.-Q. Xin, J.-F. Zhao, S.-M. Song, S.-C. Chen, Y.-B. Lu, H. Sun, High transmittance in IR region of conductive ITO/AZO multilayers deposited by RF magnetron sputtering. *Ceram. Int.* **44**, 6769–6774 (2018)
 31. Y.Y. Wang, B.J. Li, L.J. Huang, H.D. Cao, L. Zhao, N.F. Ren, Effect of Ag layer thickness and scan line spacing during laser annealing of Ag/F-doped SnO₂ bilayer composite thin films under ultrasonic vibration assistance. *J. Alloys Compd.* **829**, 154504 (2020)
 32. Y. Azizian-Kalendaragh, S. Nouhi, M. Amiri, Effect of post-annealing treatment on the wetting, optical and structural properties of Ag/Indium tin oxide thin films prepared by electron beam evaporation technique. *Mater. Express* **5**, 137–145 (2015)
 33. J. Jin, C. Liu, Z. Yang, L. Wang, The influence of AZO films on morphology and surface plasmon resonance properties of Ag particles. *Surf. Coat. Technol.* **363**, 135–141 (2019)
 34. A. Kumar, S. Mukherjee, S. Sahare, R.K. Choubey, Influence of deposition time on the properties of ZnS/p-Si heterostructures. *Mater. Sci. Semicond. Process.* **122**, 105471 (2021)
 35. R.K. Choubey, D. Desai, S.N. Kale, S. Kumar, Effect of annealing treatment and deposition temperature on CdS thin films for CIGS solar cells applications. *J. Mater. Sci. Mater. Electron.* **27**, 7890–7898 (2016)
 36. A.S.M. Maria, N. Kumaresan, K. Ramamurthi, K. Sethuraman, B.S. Moorthy, B.R. Ramesh, V. Ganesh, Influence of heat treatment on the properties of hydrothermally grown 3D/1D TiO₂ hierarchical hybrid microarchitectures over TiO₂ seeded FTO substrates. *Appl. Surf. Sci.* **449**, 122–131 (2018)
 37. T.-C. Lin, W.-C. Huang, F.-C. Tsai, Hydrogen plasma effect toward the AZO/CuCr/AZO transparent conductive electrode. *Microelectron. Eng.* **167**, 85–89 (2017)
 38. L.J. Huang, G.M. Zhang, H. Li, B.J. Li, Y.Y. Wang, N.F. Ren, Selective laser ablation and patterning on Ag thin films with width and depth control. *J. Mater. Sci. - Mater. Electron.* **31**, 4943–4955 (2020)
 39. A. Kumar, M. Kumar, V. Bhatt, D. Kim, S. Mukherjee, J.-H. Yun, R.K. Choubey, ZnS microspheres-based photoconductor

- for UV light-sensing applications. *Chem. Phys. Lett.* **763**, 138162 (2021)
40. N.M. Ahmed, F.A. Sabah, H.I. Abdulgafour, A. Alsadig, A. Sulieman, M. Alkhoaryef, The effect of post annealing temperature on grain size of indium-tin-oxide for optical and electrical properties improvement. *Results Phys.* **13**, 102159 (2019)
 41. S.G. Deshmukh, V. Kheraj, A.K. Panchal, Effect of annealing on the properties of Cu_3BiS_3 thin films deposited via chemical bath deposition. *Mater. Today: Proc.* **5**, 10712–10716 (2018)
 42. X. Liu, W. Bi, Z. Liu, Influence of post-annealing on the properties of Sc-doped ZnO transparent conductive films deposited by radio-frequency sputtering. *Appl. Surf. Sci.* **255**, 7942–7945 (2009)
 43. B.J. Li, Y.Y. Wang, L.J. Huang, H.D. Cao, Q.H. Wang, H.T. Ding, N.F. Ren, Influences of ultrasonic vibration on morphology and photoelectric properties of F-doped SnO_2 thin films during laser annealing. *Appl. Surf. Sci.* **458**, 940–948 (2018)
 44. Y. Jiang, X. Li, W. Jiang, Q. Wan, X. Gan, Y. Zhao, C. Hua, X. Li, J. Zhang, Thickness effect in laser shock processing for test specimens with a small hole under smaller laser power density. *Opt. Laser Technol.* **114**, 127–134 (2019)
 45. T.Y. Wang, B.J. Li, N.F. Ren, L.J. Huang, L. Huang, Influence of Al/Cu thickness ratio and deposition sequence on photoelectric property of ZnO/Al/Cu/ZnO multilayer film on PET substrate prepared by RF magnetron sputtering. *Mater. Sci. Semicond. Process.* **91**, 73–80 (2019)
 46. D. Scorticati, A. Illiberi, T.C. Bor, S.W.H. Eijt, T. Schut, G.R.B.E. Romer, M. Klein Gunnewiek, A.T.M. Lenferink, B.J. Kniknie, R. Mary Joy, M.S. Dorenkamper, D.F. de Lange, C. Otto, D. Borsa, W.J. Soppe, A.J. Huis in't Veld, Thermal annealing using ultra-short laser pulses to improve the electrical properties of Al:ZnO thin films. *Acta Mater.* **98**, 327–335 (2015)
 47. R.C. Chang, T.C. Li, C.W. Lin, Influence of various thickness metallic interlayers on opto-electric and mechanical properties of AZO thin films on PET substrates. *Appl. Surf. Sci.* **258**, 3732–3737 (2012)
 48. D. Gaspar, A.C. Pimentel, M.J. Mendes, T. Mateus, B.P. Falcão, J. Soares, A. Araújo, A. Vicente, S.A. Filonovich, H. Águas, R. Martins, I. Ferreira, Ag and Sn nanoparticles to enhance the near-infrared absorbance of a-Si: H thin films. *Plasmonics* **9**, 1015–1023 (2014)
 49. A. Kumar, D. Pednekar, S. Mukherjee, R.K. Choubey, Effect of deposition time and complexing agents on Hierarchical nanoflakes CdS structured thin films. *J. Mater. Sci. - Mater. Electron.* **31**, 17055–17066 (2020)
 50. Q. Wang, B. Li, F. Toor, H. Ding, Novel laser-based meta-surface fabrication process for transparent conducting surfaces. *J. Laser Appl.* **31**, 022505 (2019)
 51. R. Chen, Z. Hu, Y. Ye, J. Zhang, Z. Shi, Y. Hua, An anti-reflective 1D rectangle grating on GaAs solar cell using one-step femtosecond laser fabrication. *Opt. Lasers Eng.* **93**, 109–113 (2017)
 52. X. Chen, B. Jia, J.K. Saha, B. Cai, N. Stokes, Q. Qiao, Y. Wang, Z. Shi, M. Gu, Broadband enhancement in thin-film amorphous silicon solar cells enabled by nucleated silver nanoparticles. *Nano Lett.* **12**, 2187–2192 (2012)
 53. C.P. Burrows, W.L. Barnes, Large spectral extinction due to overlap of dipolar and quadrupolar plasmonic modes of metallic nanoparticles in arrays. *Opt. Express* **18**, 3187–3198 (2010)
 54. B.J. Li, G.Y. Yang, L.J. Huang, T.Y. Wang, N.F. Ren, Effects of BN layer on photoelectric properties and stability of flexible Al/Cu/ZnO multilayer thin film. *Ceram. Int.* **46**, 14686–14696 (2020)
 55. C.-T. Wu, Y.-R. Ho, D.-Z. Huang, J.-J. Huang, AZO/silver nanowire stacked films deposited by RF magnetron sputtering for transparent antenna. *Surf. Coat. Technol.* **360**, 95–102 (2019)
 56. B.J. Li, G.Y. Yang, L.J. Huang, W. Zu, H. Li, Y.L. Wang, S.S. Li, N.F. Ren, Surface morphology and photoelectric properties of FTO ceramic thin films under a simple transparent cover-assisted laser annealing. *Mater. Res. Bull.* **108**, 151–155 (2018)
 57. B.J. Li, Y.Y. Wang, L.J. Huang, H.D. Cao, Q.H. Wang, N.F. Ren, H.T. Ding, Ultrasonic-vibration-assisted laser annealing of fluorine-doped tin oxide thin films for improving optical and electrical properties: Overlapping rate optimization. *Ceram. Int.* **44**, 22225–22234 (2018)
 58. S. Kumar, H.C. Jeon, T.W. Kang, R. Seth, S. Panwar, S.K. Shinde, D.P. Waghmode, R.G. Saratale, R.K. Choubey, Variation in chemical bath pH and the corresponding precursor concentration for optimizing the optical, structural and morphological properties of ZnO thin films. *J. Mater. Sci. Mater. Electron.* **30**, 17747–17758 (2019)

Publisher's Note Springer Nature remains neutral with regard to jurisdictional claims in published maps and institutional affiliations.